LRP 665/00 May 2000

Understanding Sawtooth Activity During Intense Electron Cyclotron Heating Experiments on TCV

I. Furno, C. Angioni, F. Porcelli, H. Weisen,
R. Behn, T.P. Goodman, M.A. Henderson,
Z.A. Pietrzyk, A. Pochelon, H. Reimerdes

Submitted to
NUCLEAR FUSION

ISSN 0458-5895

Understanding Sawtooth Activity During Intense Electron Cyclotron Heating Experiments on TCV

I. Furno, C. Angioni, F. Porcelli[1], H. Weisen,

R. Behn, T.P. Goodman, M.A. Henderson, Z.A. Pietrzyk, A. Pochelon, H. Reimerdes

Centre de Recherches en Physique des Plasmas, Association EURATOM-Confédération Suisse,

Ecole Polytechnique Fédérale de Lausanne, CH-1015 LAUSANNE, Switzerland

[1]Istituto Nazionale Fisica della Materia and Dipartimento di Energetica,

Politecnico di Torino, I-10129 Torino, Italy

Abstract

Different types of central relaxation oscillations are observed in the presence of Electron Cyclotron Heating (ECH) depending on the location of the deposited power. In the Tokamak à Configuration Variable (TCV), normal sawteeth, i.e. triangular like Ohmic sawteeth, and saturated sawteeth are observed with central ECH power deposition, while giant sawteeth and humpback oscillations occur when heating close to the sawtooth inversion surface of the local soft X-ray emissivity. New measurements with high temporal resolution show that the crash phase of these sawtooth types is accompanied by a reconnection process associated with an $m/n = 1$ resistive internal kink mode. After the sawtooth crash, full magnetic reconnection is observed in normal and in saturated sawteeth, while for giant and humpback sawteeth the reconnection process is incomplete and poloidally asymmetric temperature profiles are observed. The detailed dynamics of the magnetic island, associated to the resistive internal kink mode, have been described by a displacement function inferred from the experimental data. In normal sawteeth, the kink mode is

destabilized just before the crash, while in all other sawtooth types a magnetic island exists for a significant fraction of the sawtooth period. The different types of sawteeth have been simulated using a numerical code based on a theoretical model which describes the evolution of the electron temperature in the presence of localized heat sources and of a magnetic $m/n = 1$ island.

1 Introduction

Sawtooth oscillations in tokamak discharges are periodic relaxations of the central electron temperature and density which develop when the safety factor on axis, q_0, drops below unity. A slow rise (sawtooth ramp) of these plasma parameters in the central region of the discharge, determined by heat deposition and transport, is followed by a rapid drop (sawtooth crash) resulting in an expulsion of energy and particles from the plasma core. Although these internal instabilities have long been observed and studied in all tokamaks, the understanding of the underlying physical mechanism is incomplete. Furthermore, recent experiments have revealed new peculiar plasma features when localized ECH is applied in sawtoothing tokamak discharges. Examples are the observation on the RTP tokamak [1] of sharp temperature gradients just outside the sawtooth inversion radius and the multipeaked temperature profiles observed in the TEXT-U [2] and RTP [1] experiments. On TCV [3], the sawtooth activity is strongly dependent on ECH deposition conditions. In Ref. [4], a classification of the different types of observed sawteeth was proposed, from usual triangular sawteeth, obtained with on-axis power deposition, to non-standard behavior when the location of the resonance position is moved off-axis. In particular, when the ECH power is deposited close to the $q = 1$ surface, the line integrated soft X-ray traces can exhibit 'humpback'-like features. These internal relaxation oscillations, which were first observed with

central electron cyclotron counter current drive [5] in the T-10 tokamak, can also occur under similar conditions on TCV [6], although current drive is not essential.

In previous TCV papers on this subject [4, 7, 8], understanding the sawtooth dynamics was hampered by the limited temporal resolution of the available diagnostics which did not allow us to resolve the sawtooth crash phase. This has now been overcome by a new soft X-ray tomographic system with improved time resolution which allows the monitoring of the sawtooth crash ~10 times faster than the crash time, which is typically ~100 μs.

In this paper, we report on these high temporal resolution measurements of the sawtooth oscillations during ECH. An interpretation of the observed phenomena is provided and linked to a recently developed theoretical model [9]. The experimental features during the different types of sawteeth are reproduced by a numerical code which is based on this theoretical model. It is shown that the sawtooth behavior is the consequence of specific features in the electron temperature profiles produced both by ECH and the advection and mixing of electron thermal energy associated with an $m/n = 1$ resistive internal kink mode [10]. Possible explanations of the remaining inconsistencies are proposed, showing that a single model can explain the variety of different sawteeth.

The remainder of the article is organized as follows. In Sec. 2, the TCV Tokamak, the ECH system and the relevant diagnostics are briefly reviewed. In Sec. 3, the experimental results and the heuristic interpretation are presented. The theoretical model is derived in Sec. 4 and the simulations of the different types of sawteeth are discussed in Sec. 5. Finally, the conclusions are summarized in Sec. 6.

2 Experimental set-up

TCV is a tokamak with major radius $R = 0.88$ m, minor radius $a = 0.25$ m, vacuum vessel elongation $\kappa = 3$ and vacuum central magnetic field $B \leq 1.43$ T. For these experiments, TCV was operated with three 82.7 GHz, 500 kW gyrotrons, with a 2 s pulse length, for heating at the second cyclotron harmonic resonance using the extraordinary mode. The 3 launching mirrors are separately orientable in the toroidal and poloidal direction. The vertical microwave beam width near the plasma center is $w = 2.5$ cm in free-space (beam intensity $\propto exp[-2(r/w)^2]$, where r is the distance transverse to the direction of the beam propagation). Local ECH power densities in excess of 10 MW/m^3 can be obtained.

The soft X-ray tomography system [11] consists of ten pinhole cameras at the same toroidal location, each equipped with a 47 μm Beryllium filter and a linear array of 20 Silicon photodiodes, which are sensitive to electromagnetic radiation in the range 1-10 keV. The system has been recently upgraded with a 16 bit data acquisition module with a 13 μs sampling rate, allowing high time resolution measurements of the sawtooth crash dynamics. The local soft X-ray emissivity distribution is reconstructed from the line integrated measurements by means of the Minimum Fisher Information regularization method [11] on a grid of 3 cm square pixels. The time sequences of the reconstructed emissivities, $S_X(r, t)$, are analysed using the Singular Value Decomposition (SVD) method [12] to obtain the spatial structures, u_k, (*topos*) and their corresponding temporal evolution, v_k, (*chronos*) such that $S_X(r, t) = \sum u_k(r) v_k(t) s_k$, where s_k are the singular values. Structures with poloidal mode numbers up to $m = 3$ are resolved by the SVD and coherent rotating structures such as MHD modes can be identified. It has been

shown [4, 13] that there is a strong correlation between the sawtooth shape and the heating location relative to the sawtooth inversion surface, in the sense that small changes in the location of the ECH deposition with respect to the inversion surface lead to large changes in sawtooth period, amplitude and MHD activity. The SVD method also provides a reliable tool in the determination of the sawtooth inversion surface of the local soft X-ray emissivity. In the following, the sawtooth inversion contours are defined by the equation:

$$\widehat{S}_X(r, t_{before}) - \widehat{S}_X(r, t_{after}) = 0. \tag{1}$$

Here, $\widehat{S}_X$ is obtained from the SVD expansion by discarding topo/chrono couples which are not poloidally symmetric, i.e. corresponding to poloidal mode numbers $m \geq 1$, and the times t_{before}, t_{after} are relative to the sawtooth crash time. The effective inversion radius is defined as $r_{inv} = \sqrt{A_{inv}/\pi}$, where A_{inv} is the cross sectional area within the inversion contour defined by Eq. (1). The size of the grid used in the tomographic reconstruction is taken as an estimate of the uncertainty in r_{inv}.

The radial displacement, $\xi(t)$, of the position of the maximum emissivity, associated with the kink instability during the sawtooth crash, is also extracted from the reconstructed soft X-ray emissivities. The time evolution of $\xi(t)$ is assumed to represent the displacement of the magnetic axis, which is not predicted theoretically by the model to be described in Sec. 4. In what follows, we define the effective displacement

$$\xi(t) = \sqrt{\kappa_0 \left[(R - R_0)^2 + \frac{(Z - Z_0)^2}{\kappa^2_0} \right]} \tag{2}$$

where (R, Z) is the position of maximum emissivity within the hot core, (R_0, Z_0) refers to the

same point before the instability develops and κ_0 is the elongation at the plasma center. From this definition, $\xi(t)$ is constant on flux surfaces and therefore can be directly compared with the effective inversion radius r_{inv}. The elongation of the magnetic flux surfaces varies little inside the $q = 1$ surface, which justifies the use of the central elongation in Eq. (2).

The soft X-ray emission is also monitored by four toroidally equispaced Silicon photodiodes (50 μm Beryllium filter, 250 kHz acquisition frequency) placed at the top of the vessel and viewing the plasma on chords intersecting the poloidal midplane at a distance about 7 cm from the center of the vessel. These are used to determine toroidal mode numbers $n = 1, 2$, assuming there is no aliasing from toroidal mode numbers $n \geq 3$.

Other diagnostics available on TCV include toroidal and poloidal arrays of Mirnov coils, a 14-channel far-infrared interferometer (FIR) and 25-point multipulse Thomson scattering system [14]. The latter provides profiles of the electron temperature and density with a spatial resolution of 40 mm in vertical direction and 3 mm in radial and toroidal directions with a typical sampling rate of 60 kHz. Using a combination of three almost co-linear laser beams, sampling intervals down to 0.4 ms can be achieved in the so-called 'burst-mode', when the three lasers are triggered close together.

The position of the ECH absorption region and the total absorbed power are determined by the ray-tracing code TORAY [15].

3 Experimental observations and heuristic understanding

In this Section, we report on high temporal resolution measurements of the various relaxation oscillations under localized and intense ECH. The injected power, P_{ECH}, exceeds the Ohmic

power by up to a factor of 4 and the microwave beam is launched perpendicular to the toroidal magnetic field. In this geometry, the amount of driven current, resulting from the magnetic field lines pitch when heating off-axis, is less than 2% of the inductive plasma current. Although it has recently been shown that a small amount of driven current can significantly change the sawtooth period and amplitude [17], this is not considered to be relevant to the physical mechanisms described in the present analysis.

Standard and saturated sawteeth, related to central heating, together with large, almost triangular sawteeth and humpback oscillations, which occur with ECH power deposited close to the sawtooth inversion surface, are analysed.

3.1 Standard sawteeth

An example of a standard, triangular sawtooth obtained with on-axis ECH power deposition is shown in Fig. 1. In what follows, the plasma parameters are referred to the Last Close Flux Surface (LCFS) which in the present case are: δ = 0.42, κ = 1.41, I_P = 400 kA, P_{ECH} = 900 kW. The sawtooth period, τ_{ST}, is ~3.4 ms and the relative crash amplitude is $\Delta S_X(0)/\bar{S}_X(0) \sim 0.65$, where the bar $\bar{}$ indicates the average of a quantity evaluated before and after the sawtooth crash. The temporal evolution of the local emissivities is shown in Fig. 1 (a, b, c) for three different radial positions together with radial displacement $\xi(t)$ of the hot core (region of high emissivity) in Fig. 1 (d). In Fig. 2, the soft X-ray emissivity distribution is shown at different times during the sawtooth collapse together with the LCFS, the sawtooth inversion radius, as calculated from soft X-ray tomography, and the hot core trajectory.

During the sawtooth ramp, the soft X-ray emissivity is poloidally symmetric, Fig. 2 (a), with no detectable MHD mode activity. At the sawtooth crash, an $m/n = 1/1$ instability grows and causes the hot core to move radially outward as a nearly rigid structure in ~120μs. The final radial shift of the hot core from the initial position is $\xi_{max} \sim 15.5$ cm. During the displacement, the hot core intensity diminishes, Fig. 2 (b), and the expelled heat redistributes on a hot ring localized, within the error bars, at the sawtooth inversion radius $r_{inv} \sim 12.3$ cm, Fig. 2 (c). The soft X-ray emissivity profile is poloidally symmetric at the end of the sawtooth crash, Fig. 2 (d). The heat redistribution on the annular ring, probably due to heat transport along magnetic field lines, appears to be much faster than the hot core radial displacement and cannot be resolved with the 13 μs time resolution of the tomographic system. Small regions of locally lower or higher emissivity at the inversion surface, visible in Fig. 2 (d) can be explained by artefacts of the tomographic reconstruction technique.

The result of the sawtooth oscillation on the soft X-ray emissivity profiles is shown in more detail in Fig. 3. The peaked pre-crash profile evolves into a hollow post-crash profile, with $S_X(\rho_{inv})/S_X(0) \sim 1.35$. The timescale of the evolution of the post-crash profile depends both on heating conditions and plasma parameters. In the present case, the hot ring is visible for ~150 μs then the profile gradually becomes more peaked as the plasma is heated until the next sawtooth collapse. Interpretation of the variation in the soft X-ray emissivity in terms of changes in the electron temperature is not straightforward. Although the Thomson scattering system provides direct measurements of T_e and n_e profiles, no measurement of the electron temperature profiles during the life-time of the hot ring have been obtained so far. This is due to the limited repetition rate and the difficulty of synchronizing the Thomson scattering laser pulses with the sawtooth

crash. A rough estimate of the hollowness in the electron temperature profile can be obtained from the soft X-ray measurements, assuming $\Delta T_e/T_e = \alpha \Delta S_X/S_X$, where $\alpha = d(lnS_X)/d(lnT_{e0})$ is the factor describing the temperature dependence of the soft X-ray emissivity of the dominant impurity, Carbon in TCV [18]. For the case shown in Fig. 3, the estimate gives $T_e(r_{inv})/T_{e0} \sim 1.2$, assuming flat electron density, n_e, and Z_{eff} profiles. Abel inverted interferometric measurements show that particles are expelled from the plasma center ($\Delta n_e(0)/\bar{n}_e(0) \sim 0.09$), during the sawtooth crash, resulting in a flattening of the n_e profile with $n_e(r_{inv})/n_e(0)$ below the error bars (5%) of the inversion technique. Since there is no independent measurement of the Z_{eff} profile during the lifetime of the hot ring, we cannot exclude the possibility that a local enhancement of Z_{eff} at the hot ring position may contribute to the soft X-ray intensity. Such an enhancement could result from a highly peaked Z_{eff} profile in the plasma core before the sawtooth crash. The Z_{eff} profile can be obtained from simultaneous soft X-ray, T_e and n_e measurements in the manner proposed in Ref. [19]. This has been done for the present case and pre-crash Z_{eff} profiles, which are flat inside the inversion radius were obtained. This result does not support the existence of impurity accumulation and hence makes it implausible that the hot ring emissivity is due to an enhanced impurity density inside the ring.

In Sec. 5, it will be shown that the formation of the hot ring can be explained as a consequence of the advection and mixing of the electron thermal energy during the growth of the $m/n = 1$ magnetic island. However, the hot ring only forms when the pre-crash temperature profile is sufficiently peaked, as in the case for on-axis ECH deposition. With Ohmic heating only, this condition is normally not fulfilled and the hot ring is not observed.

The absence of post-cursor oscillations on both Mirnov coils and soft X-ray traces suggests a full

reconnection process, in the sense that poloidal magnetic symmetry is restored at the end of the sawtooth crash. This requires that the original magnetic axis moves up to the mixing radius, r_{mix}, at the end of the reconnection process, i.e. $\xi_{max} \cong r_{mix}$ (See Sec. 4, for the mathematical definition of r_{mix}). This radius is slightly larger than the sawtooth inversion radius, by an amount which depends on the safety factor and electron temperature profiles before the crash (See Appendix in [4]). The maximum value of the hot core displacement, $\xi_{max} \sim 15$ cm, compared with $r_{inv} \sim 12$ cm, is consistent with this interpretation.

3.2 Saturated sawteeth

Tomographic reconstructions of a saturated sawtooth are shown in the second example from TCV discharge 14385 with central ECH. Plasma parameters are: $\delta = 0.37$, $\kappa = 1.46$, $I_p = 266$ kA, $P_{ECH} = 850$ kW. The EC resonance position is located on the magnetic axis with a radial power deposition width, $\delta_{abs} \sim 6$ cm. This discharge has a lower current than the previous case with a consequently smaller inversion radius of $r_{inv} \sim 9$ cm. In Fig. 4, the temporal evolution of the tomographically inverted soft X-ray emissivity at different radial positions is shown together with the hot core radial displacement, $\xi(t)$.

The sawtooth crash is followed by a reheating phase, in which the soft X-ray emissivity profiles peaks, conserving the poloidal symmetry. This phase is followed for $t > 0.965$ s by a saturated phase during which the central soft X-ray emissivity remains almost constant or even decreases until the following sawtooth crash. The saturated phase is accompanied by strong mode activity, resulting in oscillations visible off-axis, Fig. 4 (b). The frequency of the oscillations (in the present case ~6 kHz) can vary between 3 and 7 kHz, depending on ECH and plasma conditions. Close to

the inversion radius, Fig. 4 (d), a frequency doubling is sometimes observed. During the saturated phase, the plasma hot core appears to rotate around its position at a distance $\xi \sim 1$ cm.

In Fig. 5, the mode structure of the soft X-ray emissivity, from SVD analysis, is shown in a small time window during the saturated phase, highlighted in yellow in Fig. 4 (a). The first topo/chrono pair, corresponding to the largest singular value, is not shown because it describes the temporal evolution of the average emissivity profile and thus is not relevant to the mode identification. Inspection of Fig. 5 reveals the presence of two rotating modes, each consisting of two oscillating topo/chrono pairs in quadrature (i. e. both topo and chrono are phase shifted by $\pi/2$) and having poloidal mode numbers $m = 1$ (topo/chrono pairs $k = 2, 3$) and $m = 2$ (topo/chrono pairs $k = 4, 5$). Both modes rotate in the electron diamagnetic drift direction at a frequency of ~6 kHz and their maxima and minima are located at the sawtooth inversion radius, within experimental uncertainties. The toroidal mode number, n, as obtained from the toroidal photodiodes, is such that $m/n = 1$.

The saturation phase terminates with the sawtooth crash when the rapid growth of the $m/n = 1/1$ mode causes the hot core to move within 80 μs, see Fig. 4 (d). Fig. 6 shows different soft X-ray emissivity profiles, at times corresponding to the arrows indicated in Fig. 4, together with the location of the sawtooth inversion radius. The poloidal symmetry is restored and the soft X-ray emissivity profile is seen to flatten up to $r = r_{inv}$ at the end of the sawtooth crash. The relative crash amplitude is less pronounced for a saturated than for a standard sawtooth. In the present case $\Delta S_X(0)/\bar{S}_X(0) \sim 0.28$.

The lack of post-cursor oscillations on both soft X-ray traces and Mirnov coil signals again suggests a full reconnection process. The absolute value of the displacement, $\xi_{max} \sim 7$ cm, compared with

the inversion radius, $r_{inv} \sim 9.3$ cm, may be too small to explain a complete mixing of the plasma core inside r_{mix}. However, it should be noted that in the very last phase of the reconnection process the maximum of the emissivity profile may no longer be at the position of the displaced magnetic axis in the hot core, making the determination of the displacement function, ξ, difficult.

3.3 Heating close to the sawtooth inversion surface

In earlier ECH experiments on TCV [4], it was observed that small changes in the relative position between the ECH location and the sawtooth inversion surface can lead to large changes in the sawtooth shape, period and MHD activity. More recent experiments with three independent gyrotrons heating close to the sawtooth inversion surface suggested that even the beam width may play a role in determining the sawtooth shape [17]. In particular, two types of sawteeth are observed when the power is deposited close to the sawtooth inversion surface: large, almost triangular sawteeth, which we shall refer to as giant sawteeth, and non-standard sawteeth which were termed humpback oscillations when they were observed in the T-10 tokamak [5]. A detailed study of the plasma parameters and heating conditions under which giant sawteeth occur, rather then humpbacks, has already been presented [4, 8, 17]. In what follows, an experimental account of the two types of sawteeth is presented and an interpretation of the observed behavior is given. Despite the strong difference in the soft X-ray signals in the two types of sawteeth, we show that the gross features of the electron temperature behavior and the MHD activity are similar and that they result from the combined action of local ECH and a saturated magnetic island.

The sawtooth behavior for giant sawteeth and the humpback oscillations is presented in Fig. 7 and Fig. 8 respectively. In both figures, the temporal evolution of the central soft X-ray emissivity,

$S_X(0)$, is shown in frame (a), together with the central electron density, $n_e(0)$, from Abel-inverted interferometer measurements, (b). The quantity $\tilde{T}_{e0} = S_X(0)/n_e^2(0)$, in frame (c), is indicative of the evolution of the central electron temperature (the exponent α, introduced above is close to unity in the present cases).

We examine the giant sawtooth case for which the plasma parameters are: $\delta = 0.5$, $\kappa = 1.47$, $I_p = 330$ kA, $q = 3.25$, $P_{ECRH} \sim 500$ kW. The ECH absorption layer is located in the plasma midplane on the high field side of the magnetic axis inside the interval $r/a = [0.55, 0.65]$. The sawtooth inversion surface is located at the normalized radius $r_{inv}/a = 0.6$. In Fig. 9, the electron temperature and density profiles are shown for the different times indicated by letters A-C in Fig. 7. In this case, the Thomson scattering lasers were operated in the 'burst-mode' to obtain 3 profiles in a few milliseconds.

The sawtooth period, $\tau_{ST} \sim 15$ ms, is significantly longer then the standard sawtooth period. During a single sawtooth period, three distinct phases can be identified during which $\tilde{T}_{e0}$ shows different temporal behavior (Fig. 7 (c)). At the sawtooth crash, $\tilde{T}_{e0}$ is observed to drop on a fast time scale, typically $\tau_{crash} < 0.1$ ms. The pre-crash electron temperature profile (Fig. 9, profile A) is relatively flat inside the sawtooth inversion surface and the sawtooth crash results only in a small variation of the central electron temperature. Both the central soft X-ray emissivity and electron density also drop during the crash phase. For instance, in Fig. 7, $\Delta S_X(0)/\bar{S}_X(0) \sim 0.66$ and $\Delta n_e(0)/\bar{n}_e(0) \sim 0.48$. The tomographic reconstructions of the soft X-ray emissivity (not shown here) and the electron temperature profile (see Fig. 9, B) show that the poloidal symmetry is not restored after the sawtooth crash, suggesting an incomplete reconnection process.

The sawtooth crash is followed by a ramp phase during which the central electron temperature

and density increase. The time scale of this phase, typically $\tau_{ramp} \sim 2$ ms, is slower then τ_{crash} and is the same as that of triangular sawteeth with central ECH deposition and comparable ECH power, safety factor and plasma energy content. The electron temperature profile C, (Fig. 9), shows that the poloidal symmetry is not restored during the ramp phase which terminates with the onset of strong oscillations in the soft X-ray traces (highlighted in yellow in Fig. 7). Typical oscillations in the soft X-ray signals due to the presence of a saturated magnetic island are not easy to distinguish early in the sawtooth ramp since the time scale of the rise is close to the rotation frequency of the mode which produces the oscillations (see below). In Fig. 10, the mode structure of the soft X-ray emissivity during the oscillations is shown: a mode (Fig. 10, topos/chronos 2, 3) having poloidal mode number $m = 1$ and rotating in the electron diamagnetic drift direction at a frequency of ~1.5 kHz is clearly present. The toroidal mode number is $n = 1$. The sawtooth ramp is followed by a diffusive phase during which the central electron temperature undergoes small changes on an even slower time scale ($\tau_{slow} \sim 10$ ms). During this phase, a strong influx of particles into the plasma core is seen, leading to a very peaked electron density profile. The profiles are poloidally symmetric and the electron temperature profile is flat inside the sawtooth inversion radius at the end of the sawtooth ramp. This phase lasts until the onset of precursor oscillations ~500 μs before the subsequent sawtooth crash.

Fig. 8 shows the humpback oscillation which can occur when heating close to the sawtooth inversion surface. The plasma parameters are: $\delta = 0.2$, $\kappa = 1.37$, $I_p = 200$ kA, $q = 4.8$, $P_{ECRH} \sim 700$ kW. The ECH resonance position is located below the magnetic axis resulting in a comparatively broader absorption layer located inside the region $r/a = [0.2, 0.4]$. The sawtooth

inversion surface is located at the normalized radius $r_{inv}/a = 0.32$.

For the humpback case, like for the giant sawteeth, τ_{ST} is significantly longer than the standard sawtooth period, $\tau_{ST} \sim 8$ ms. At first sight, the evolution of the central soft X-ray emissivity in the humpback case suggests that the electron temperature behavior is radically different from that of the giant sawteeth. However, as can be seen from Fig. 8 (c), the temporal evolution of the central soft X-ray emissivity is mainly dependent on $\tilde{T}_{e0}$, since $n_e(0)$ has only small variations (1-2%) during a sawtooth period in the humpback case, as compared with the large variations of the density during the giant sawteeth. When this difference in the density behavior is accounted for, the $\tilde{T}_{e0}$ evolution is very similar. The three timescales of evolution of $\tilde{T}_{e0}$, found in the giant sawtooth case, also apply to the humpback oscillations and a detailed analysis of each of these phases, as previously performed for the giant sawtooth, reveals the same MHD mode structure.

The difference in the electron density behavior between giant sawteeth and humpback oscillations is not yet understood, nevertheless we suppose that it can be ascribed to the 'pump-out' effect observed when ECH power is deposited inside the sawtooth inversion region under certain plasma and heating conditions [20]. In the case of the humpback oscillations, this condition is fulfilled, possibly because of the broad ECH absorption region such that a considerable amount of the power is deposited inside the sawtooth inversion region. The giant sawteeth show a particle influx during the sawtooth ramp which is comparable to that observed for triangular sawteeth with central heating. In contrast, during humpback oscillations the pump-out particle flux may prevent the electron density profile from peaking. Deposition inside r_{inv} appears to be a necessary, but not a sufficient condition for the appearance of the pump-out since triangular sawteeth with central deposition have a normal density behavior.

Our understanding of the electron temperature behavior, in both sawtooth types described above, is based on the following heuristic picture. When the ECH power is deposited near the sawtooth inversion surface, the electron temperature profile tends to acquire distinctive features. In particular, T_e becomes relatively flat (see Fig. 9, T_e profile A), possibly even hollow, in the central region up to the $r = r_{inv}$ and relatively steep outside this radius, as the result of localized heating and diffusive transport during a period of relative MHD quiescence. Since the formation of these features in the electron temperature profile requires a relatively long quiescent period, improved stability against $m/n = 1/1$ modes is an important factor. This improvement is possible because ECH power deposited sufficiently near the $q = 1$ surface can lead to a reduced magnetic shear near that surface (via an increase of the local electrical conductivity and hence current density), which is known from experiments [21, 22, 23] and theory [24] to have a stabilizing influence. This period is terminated by the appearance of an $m/n = 1/1$ magnetic island [10, 25], indicated by brief precursor oscillations in the soft X-ray traces. In this first phase, so long as magnetic reconnection takes place, the island moves radially outwards and the soft X-ray emissivity decreases. The magnetic topology during this phase (Fig. 12) is such that crescent-shaped surfaces inside the magnetic island separatrix directly connect the heated ring with the plasma center. Therefore, the central plasma region is still heated even though radially separated from the ECH deposition region due to the large thermal conduction along field lines. When the hot core starts to move outwards again and the reconnection process continues, the central temperature remains almost constant. The brief oscillations present in the experimental traces in this phase are in agreement with the existence of an $m/n = 1$ mode and the picture of a magnetic island which is now close to the mixing radius, with the reconnection process close to

completion. Subsequently, the poloidal symmetry is re-established and no further oscillations are seen in the soft X-ray signals.

4 Theoretical model

Many of the experimental results in the previous section can be interpreted using a theoretical model, first presented in Ref. [9], which describes the evolution of the electron temperature in the presence of $m/n = 1$ magnetic island and localized heat sources. The derivation of this model is detailed in this Section.

The part of the model that describes the evolution of $m/n = 1$ magnetic islands is fairly standard and the evolution of these islands is assumed to follow the characteristic spatial structure of a resistive internal kink mode [10] and the topological constraints of Kadomtsev's model [25]. Although this model is fairly old, its consequences in the presence of localized auxiliary heating have only recently been fully appreciated. In Ref. [9], it was proposed that the temperature "filamentary" structures and sharp gradients observed in RTP [1] and in TEXT-U [2] are consistent with the Kadomtsev's model. In this paper, we show that the model may also account for the variety of experimental observations in sawtoothing TCV discharges, although we do not strictly follow Kadomtsev's model.

We do not use Kadomtsev's prediction for the timescale of the sawtooth crash. This prediction would be valid for a plasma obeying resistive MHD equations [26]. High temperature tokamak experiments, such as TCV, are ill-described by resistive MHD. For instance, TCV is better described by a semi-collisional kinetic model [4], where diamagnetic and ion Larmor effects are important for the island evolution. Toroidal effects, not treated by Kadomtsev, are also important.

Unfortunately, a fully consistent non-linear theory for the island dynamics that accounts for all these effects is not yet available. Therefore, the model used contains a free parameter, which describes the evolution of the $m/n = 1$ magnetic island width, or alternatively, of the displacement function $\xi(t)$ which can now be measured experimentally, as shown in Sec. 3.

The original Kadomtsev's model assumes full magnetic reconnection. Single-helicity, $m/n = 1$ island growth occurs until this island reaches its maximum amplitude, $w_{max} = 2r_{mix}$, where the mixing radius, r_{mix}, is defined below. We suspect that the single-helicity assumption is not valid in a strict sense in a three-dimensional toroidal system. Satellite harmonics of the internal kink magnetic perturbation, such as the $m/n = 2/1$ harmonic driven by toroidal coupling, will cause some degree of magnetic stochasticity [27]. This, in turn, will cause the decoupling of the electron pressure and q profiles: the pressure may flatten in the stochastic region independently of the q profile. This would lead to incomplete reconnection and may explain why the safety factor on axis, q_0, is observed to remain below unity after the sawtooth crash in certain tokamak experiments [28, 29]. According to this picture, the extent of the stochastic region determines the degree of departure from complete reconnection. For small departures, the model presented here may satisfactorily reproduce gross features of the experimental observations. Conversely, we are tempted to conclude that if the model results agree with the experimental data, then full reconnection is really obtained in the experiment. A direct measurement of the q profile would settle this issue, but unfortunately the safety factor profile is not available on TCV.

4.1 Derivation of the model

We assume, for simplicity, a cylindrical plasma column of length L with periodic boundary

conditions. In absence of an $m/n = 1$ island, magnetic flux surface cross sections are concentric circles of constant normalized helical flux,

$$\Psi_{*in}(r) = \int_0^{r^2} [q_{in}(x)^{-1} - 1]dx \tag{3}$$

where the subscript "in" stands for initial, i.e. before the island formation. An elliptical deformation of the flux surfaces with constant elongation can be introduced trivially if desired. For a typical case (i.e. monotonic q profile), $\Psi_{*in}(r)$ has a maximum at the $q = 1$ radius, $r = r_s$, as shown in Fig. 11 (a).

Our problem is now to specify the helical flux function, $\Psi_{*in}(r, \alpha, t)$, during the growth of the $m/n = 1$ island, where $\alpha = \vartheta - 2\pi z/L$, ϑ being the poloidal angle. We note that this function is not explicitly determined in Kadomtsev's paper [25], where only $\Psi_{*rel}(r)$ is derived as a function of $\Psi_{*in}(r)$, with the subscript "rel" referring to the relaxed helical flux at the full reconnection. Nevertheless, the two basic rules for the reconstruction of $\Psi_{*in}(r, \alpha, t)$ are to be found in that paper. These rules are: (i) helical flux conservation, i.e. $\frac{\partial}{\partial t}\Psi_* + \boldsymbol{v} \cdot \nabla\Psi_* = 0$, which describes the evolution of Ψ_* everywhere except in a narrow layer around the island X-point where magnetic reconnection occurs, and (ii) toroidal flux conservation. These rules do not define a unique solution for the functional $\Psi_{*in}(r, \alpha, t)$, although they represent a strong mathematical constraint. A prescribed model for the velocity field, $\boldsymbol{v}$, is assumed corresponding to a resistive internal kink motion. Accordingly, helical flux surfaces within the $q = 1$ surface are shifted rigidly. The motion is thus specified by a single function, $\xi(t)$, representing the radial displacement of the magnetic axis from its original position. The assumption of a given velocity field greatly simplifies the analysis, but is not fully self-consistent with the solution of the set of resistive MHD

equations. An improved analytical model was the one proposed by Waelbroeck [30]. Alternatively, the resistive-MHD equations could be solved numerically, which is not the spirit of the present analysis.

According to the procedure outlined above, at each time t during the reconnection process, the island separatrix is formed by two circles of radii $r_{1sp} < r_s$ and $r_{2sp} > r_s$, where $\Psi_{*in}(r_{1sp}) = \Psi_{*in}(r_{2sp})$, with the center of the inner circle (i.e. the original magnetic axis) displaced from its original position by a distance

$$\xi(t) = r_{2sp} - r_{1sp} \tag{4}$$

(see Fig. 12). With $B_z = const$, toroidal flux conservation is equivalent to area conservation. Thus, the area A_X enclosed by the magnetic separatrix equals that of the annular region between the initial position of the two reconnecting circles, i.e. $A_X = \pi(r^2_{2sp} - r^2_{1sp})$.

The magnetic island has a width

$$w_{isl}(t) = 2\xi(t). \tag{5}$$

At a later time, the island separatrix evolves into a crescent-shaped surface, maintaining a constant area A_X indicated by the dashed regions in Fig. 11 (d). The contour of the crescent is also a surface of constant helical flux, specifically

$$\Psi_{*in}(r, \alpha, \xi) = \Psi_{*in}(r_{1sp}) \tag{6}$$

where the function Ψ_* now depends on time through $\xi(t)$. Eventually, at full reconnection when poloidal symmetry is restored, each reconnected surface becomes a circle of radius r_k such that

$\pi r_k^2 = A_x$, or

$$r_k^2 = r^2{}_{2sp} - r^2{}_{1sp} \tag{7}$$

The relaxed helical flux must satisfy the relationships

$$\Psi_{*rel}(r_k) = \lim_{\xi \to r_{mix}} \Psi_* \Big|_{r = r_k} = \Psi_{*in}(r_{1sp}) \tag{8}$$

The magnetic axis of the initial configuration reconnects with the flux surface at $r = r_{mix}$, such that

$$\Psi_{*in}(0) = \Psi_{*in}(r_{mix}) . \tag{9}$$

This formula defines the mixing radius. Observe that, at full reconnection, the initial magnetic axis and the island O-point annihilate each other, while the new axis of the relaxed configuration corresponds to the O-point of the expanding $m/n = 1$ island.

So far, we have specified the constraints that the function Ψ_* must obey but we have not derived this function explicitly. This is done now in two steps. In the first step, we find convenient to introduce a Hamiltonian function, $H = H(\Psi_*) = H(r, \alpha, \xi)$, whose constant energy contours correspond to the crescent-shaped surfaces within the island separatrix. This region is indicated as "region III" in Fig. 12. A suitable choice for this function is

$$H = \frac{(r^2 + \xi^2 - r^2{}_{1sp} - 2r\xi cos\alpha)(r_{2sp}^2 - r^2)}{r^2 + \xi^2 - 2r\xi cos\alpha} \tag{10}$$

The parameters r_{1sp} and r_{2sp} can readily be obtained as a function of $\xi(t)$ and $\Psi_{*in}(r)$, both assumed as given. The island separatrix for a given ξ corresponds to the contour level $H = 0$,

while H reaches a maximum value, $H_{max}(\xi)$, on the island O-point. Crescent-shaped surfaces correspond to contour levels $H = H_0 \in [0, H_{max}]$. Note that the curves $H(\alpha, r, t) = H_0$ become circles in both the limits $\xi = 0$ and $\xi = r_{mix}$ (in the latter limit, $r_{1sp} = 0$).

In the second step, the function $A = A(H, \xi)$ can be evaluated numerically after computing the area, A_X, pertaining to each $H = H_0$ surface; from this, using the area conservation rule, the function $\Psi_* = \Psi_*(H)$ can be constructed. A simple analytic fit can also be obtained:

$$A(H, \xi) = A_x(\xi)\left(1 - \frac{H}{H_0}\right) \tag{11}$$

For an inverse parabolic q profile,

$$\frac{q_0}{q_{in}(r^2)} = 1 - \Delta q\left(\frac{r}{r_s}\right)^2 \tag{12}$$

where $\Delta q = 1 - q_0$ is positive definite, we get [25]

$$\Psi_{*rel}(r^2) = \frac{\Delta q}{2q_0} r^2{}_s\left(1 - \frac{r^4}{4r^4{}_s}\right) \tag{13}$$

and through Eqs (6)-(8) and (11).

$$\Psi_*(\alpha, r, \xi) = \frac{\Delta q}{2q_0} r^2{}_s\left\{1 - \frac{A^2{}_x(\xi)}{4\pi^2 r^4{}_s}\left[1 - \frac{H(\alpha, r, \xi)}{H_0(\xi)}\right]^2\right\} \tag{14}$$

This function Ψ_* is valid within the island region III of Fig. 12. In regions I and II, the magnetic surface cross sections and the function Ψ_* are trivially determined from $\Psi_{*in}(r)$.

Let us now derive an equation for the electron temperature, T_e. Since in a magnetized, high temperature plasma the heat transport along magnetic field lines is large compared to the transport perpendicular to magnetic field lines, the electron temperature is constant on magnetic flux

surfaces, i.e. $T_e = T_e(\Psi_*, t)$. Similarly, since electron parallel diffusion is very large, we may conclude that $n_e = n_e(\Psi_*, t)$. Surfaces of constant Ψ_* move with the fluid and it is convenient to express the heat transport equation in a Lagrangian frame. We consider the limit of intense electron heating and relatively low density, where the collisional energy transfer between electrons and ions can be neglected. This is certainly the case in TCV with intense ECH, where the electron temperature can exceed the ion temperature by a factor of 10. The relevant equation becomes

$$\frac{3}{2} n_e \frac{\partial T_e}{\partial t} = -\nabla \cdot \boldsymbol{q} + S \tag{15}$$

where S is the heat source and

$$\boldsymbol{q} = -n_e \cdot \chi_\perp \nabla_\perp T_e \tag{16}$$

is the heat flux, with $\chi_\perp$ the perpendicular heat diffusion coefficient. The flux surface averaging (denoted by angular brackets) of Eq. (15) gives

$$\frac{3}{2} n_e \frac{\partial T_e}{\partial t} = \langle \nabla \left(n_e \chi_\perp \frac{\partial T_e}{\partial \Psi_*} \nabla \Psi_* \right) \rangle + \langle S \rangle \tag{17}$$

This equation is coupled to the equation for the electron density, which reads

$$\frac{\partial n_e}{\partial t} = \langle \nabla \left[\left(D_\perp \frac{\partial n_e}{\partial \Psi_*} - \frac{n_e v_{Pe}}{|\nabla \Psi_*|} \right) \nabla \Psi_* \right] \rangle \tag{18}$$

where $D_\perp$ is the electron diffusion coefficient across the field lines and v_{Pe} is the pinch velocity. Equations (17) and (18) describe the evolution of the electron density and temperature on magnetic flux tubes frozen to the plasma flow. At a particular instant in time when two flux tubes with equal helical flux reconnect, mixing rules for the particle density and thermal energy density must be

implemented which means that both the temperature and the density evolve during the reconnection process even if $\chi_\perp = S = 0$.

The mixing rules are derived from particle and energy conservation relations. Particle conservation can be written in integral form:

$$\int_A n_e(A')dA' = \pi \int_{r_1^2}^{r_2^2} n_{in}(r^2)dr^2 \tag{19}$$

where, as before, A is the area between two circles with equal helical flux before they reconnect. After the reconnection, A is the area of the crescent-shaped surface with the same value of Ψ_*. Differentiating Eq. (19), we obtain

$$n_e[A(\Psi_*)] = \pi\left[n_e(r_{2sp}^2)\frac{dr^2{}_{2sp}}{dA} - n_e(r_{1sp}^2)\frac{dr^2{}_{1sp}}{dA}\right] \tag{20}$$

where the metric elements $dr^2{}_{1sp}/dA$ and $dr^2{}_{2sp}/dA$ can be obtained from the initial $\Psi_{*in}(r)$. For instance, for the inverse parabolic q profile in Eq. (12), one finds

$$dr^2{}_{1sp}/dA = dr^2{}_{2sp}/dA = 1/2\pi. \tag{21}$$

The mixing rule for the thermal energy is obtained with similar considerations. However, we should consider that magnetic energy is transformed into heat during the reconnection process. A simple calculation shows that typically the transformed magnetic energy is smaller than the energy associated with the equilibrium poloidal magnetic field by two orders of magnitude and therefore can be neglected. Thermal energy conservation gives

$$p_e[A(\Psi_*)] = \pi\left[p_e(r^2_{2sp})\frac{dr^2}{dA}_{2sp} - p_e(r^2_{1sp})\frac{dr^2}{dA}_{1sp}\right] = n_e(\Psi_*)T_e(\Psi_*) \qquad (22)$$

Since $p_e = n_e T_e$, equations (20) and (22) can be combined to give the mixing rule for the electron temperature.

The appropriate boundary conditions for the temperature are as follows: an initial temperature $T_e(r, t = 0) = \tilde{T}(r)$, where $\xi(t = 0) = 0$; a condition at the plasma edge, $r = a$, located in region II of Fig. 12, normally $T(a, t) = 0$; the geometrical conditions $\partial T_e/\partial\tilde{r}|_{I,II} = 0$, where $\tilde{r}$ is the distance from the magnetic axis in the two regions. Finally, a condition at the separatrix is required. Note that, with $\chi_\perp = 0$, a discontinuity of n_e and T_e across the separatrix is in general allowed by Eq. (22). With finite $\chi_\perp$, a common temperature is found, approaching the separatrix from any of the three regions I, II, III. This common temperature is determined by the continuity of the heat flux. The boundary conditions for the density are similar. Equations (17), (18), (20), (22) with the appropriate boundary conditions and the determination of the helical flux function, as described above, completely specify the theoretical model.

In applying our model to the interpretation of the TCV experimental results, a number of simplifying assumptions was made:

• Rigid plasma toroidal rotation, with a period τ_{rot};

• The ECH power source, S, is located on the poloidal midplane between radii, r_{h1}, r_{h2} (Fig. 12); the radial width is dominated by the height of the wave beam. Over timescales longer than the rotation period, τ_{rot}, the heated region in the plasma rest frame is a ring in the poloidal cross-section, indicated by the dashed-dotted lines in Fig. 12. The region obtained by rotating the heated

ring in the toroidal direction has a volume V_h. Thus, in the plasma frame, we take for simplicity

$$S = \rho\mathcal{H}[(r-r_{h1})(r_{h2}-r)] \tag{23}$$

where $\mathcal{H}$ is the Heaviside function and $\rho = P_{ECH}/V_h$. Since parallel heat conduction is dominant, the deposited heat spreads rapidly over all flux tubes intersecting the heated ring. Thus, if we denote by dA the cross-sectional area of a generic flux tube and by dI its intersection with the heated ring, we can write the ECH power density averaged over flux surfaces as $\langle S\rangle(A) = \rho dI/dA$. Note that the heat is transported radially by parallel diffusion in a complex magnetic structure, such as that of Fig. 12, resulting in an apparent non-local transport process.

• The perpendicular heat diffusion coefficient, $\chi_\perp$, is taken to be of the form

$$\begin{cases} \chi_\perp = \left(\dfrac{r}{a}\right)^\beta \chi_{max} & \text{for } r \geq r_{2sp} \\ \chi_\perp = \left(\dfrac{r_{2sp}}{a}\right)^\beta \chi_{max} = \text{const} & \text{for } r < r_{2sp} \end{cases} \tag{24}$$

with χ_{max} and β constant parameters; $r \geq r_{2sp}$ corresponds to the region II of Fig. 12, where $\Psi_* = \Psi_{*in}(r)$.

• The initial q profile is taken as parabolic, Eq. (12). Note that this profile is used only up to $r = r_{mix}$; for this profile, $r_{mix} = \sqrt{2}r_s$. For $r \geq r_{mix}$, the magnetic topology is unchanged and the q profile can differ from inverse parabolic. The precise value of q_0 is found not to affect the resulting temperature evolution. Electron cyclotron current drive effects are neglected.

• The electron density profile is flat inside the mixing radius and fixed during the sawtooth period. This is the crudest of all our simplifications. It is justified on the basis that, with intense ECH, the electron temperature profile tends to become rather peaked and, during a sawtooth period,

$\Delta T_e/T_e \gg \Delta n_e/n_e$. This condition is satisfied for the standard and saturated sawteeth discussed in Sec. 3, but it is only marginal for the humpback oscillations and giant sawtooth.

• The temperature profile at $t = 0$ is chosen to be $T(r, t = 0) = T_0\left(1 - \frac{r^2}{a^2}\right)$, with $T_0 = 1$ keV. However, after an initial transient, which may last for a few sawtooth periods, the temperature evolution settles into a periodic cycle independent of $T(r, t = 0)$.

5 Simulation results

Numerical simulations are discussed in this Section. The parameters used in the simulations are given in Table 1.

Table 1: Simulation parameters

Simulation	r_{h1}/r_{mix}	r_{h2}/r_{mix}	χ_{max} [m^2/s]	β	P_{ECH} [kW]
Standard Sawtooth	0	0.25	3.5	1.8	500
Saturated Sawtooth	0	0.25	10.5	3	460
Deposition on $q = 1$	0.55	0.8	4.8	2	450

5.1 Standard sawtooth

Figure 13 presents the simulation of a standard, triangular sawtooth. The function $\xi(t)$ is taken to be zero for $0 \le t \le 0.975 \cdot \tau_{saw}$ and then to increase linearly up to r_{mix} during the crash, i.e. for $0.975 \cdot \tau_{saw} \le t \le \tau_{saw}$, consistent with the experimental displacement function shown in Fig. 1. Figure 13 shows local temperature traces and Figure 14 the simulated temperature profiles at the sawtooth times indicated in Fig. 13. The most striking experimental feature reproduced by our simulation is the formation of a hot ring in the relaxed temperature profile. This is not

observed in Ohmic standard sawteeth, but it occurs with intense central ECH when the pre-crash temperature profile is very peaked. This is a straightforward consequence of Kadomtsev's full reconnection model. If the crash phase is very rapid, as in the case discussed here, diffusion and heating can be neglected during this phase. Assuming a constant density profile, a pre-crash q profile as in Eq. (12) and a parabolic temperature profile before the crash a simple analytic calculation yields a relaxed temperature profile constant up to $r = r_{mix}$ and equal to the value of the pre-crash temperature at the $q = 1$ surface, corresponding to common understanding. However, if the pre-crash temperature profile is more peaked than parabolic, the relaxed profile is hollow, with a maximum at $r = r_{mix}$.

For a flat density profile and a pre-crash temperature profile

$$T_{in}(r) = T_0\left(1 - \frac{r^2}{a^2}\right)^2 \tag{25}$$

the relaxation process yields a hollow profile which can be determined analytically:

$$T_{rel}(r) = T_{in}(r_1) + T_0\left[\frac{r^4}{4a^2(a^2 - r_s^2)}\right] \text{ for } r \le r_{mix} \tag{26}$$

For $r > r_{mix}$, $T_{rel}(r) = T_{in}(r)$. Note that the relaxed temperature profile has a discontinuity at $r = r_{mix}$ which would be smoothed out by perpendicular heat diffusion.

5.2 Saturated sawtooth

Saturated sawteeth can be obtained with our model with central or slightly off-axis heating, provided the heat is deposited well within the $q = 1$ radius, Fig. 15, with the simulation parameters in Table 1. The key to obtaining saturated sawteeth is to assume a displacement function

which moves the magnetic axis early in the sawtooth ramp, by a distance comparable to the outer radius of the heat deposition region. In this way, the heating power is no longer deposited near the magnetic axis. Consequently, the electron temperature saturates at the plasma center, i.e. at the original position of the magnetic axis before the onset of the $m/n = 1$ island. The displacement function used for this simulation, shown in Fig. 15 (d), was chosen to reproduced the experimentally measured displacement, Fig. 4.

With a magnetic island width, $w_{isl} = 2\xi$, the temperature profile is not poloidally symmetric. In the presence of toroidal plasma rotation, this gives rise to oscillations of the simulated electron temperature traces, Fig. 15 (b, c). Of particular interest is the doubling of the oscillation frequency, in good agreement with the experimental traces, Fig. 4.

5.3 Deposition close to the sawtooth inversion surface

Recent attempts to simulate the humpback oscillations [31], using the same model, resulted in a sawtooth shape in which the drop and rise of the central electron temperature occur on the same timescale. This was mainly due to the choice of the displacement function, $\xi(t)$, and to the assumption of full magnetic reconnection after the sawtooth crash. This condition was, however, not fulfilled in the two examples presented in Sec. 3. In the present simulation, the function $\xi(t)$ shown in Fig. 16 (b) increases rapidly up to $0.5 \cdot r_{mix}$ during the crash and then remains constant during the sawtooth ramp, i.e. for $0 \le t \le 0.3 \cdot \tau_{saw}$. After the sawtooth ramp, for $0.3 \cdot \tau_{saw} \le t \le 0.4 \cdot \tau_{saw}$, $\xi(t)$ reaches the mixing radius completing the reconnection process. The ECH power is deposited on the $q = 1$ surface and the parameters are given in Table 1. The main features of experimental sawtooth traces are reproduced. In particular, the overall evolution

of the central electron temperature is in agreement with the time traces shown in Fig. 7 and Fig. 8. The three distinct phases with different timescales, previously described, are correctly reproduced by the simulation and the electron temperature profiles are qualitatively consistent with the Thomson scattering measurements, Fig. 9.

6 Conclusions

In the TCV tokamak, different types of sawtooth oscillations, ranging from triangular to non-standard sawteeth, are observed in the presence of ECH as the location of the power deposition is moved from the magnetic axis to the sawtooth inversion surface. Measurements with high temporal resolution have shown that the different sawtooth shapes and their features in the electron temperature profiles are compatible with the strong localization of the heating region, which is specific to the ECH method, and of the advection and mixing of electron thermal energy associated with a resistive internal kink mode. This mode produces precursor oscillations which have been identified to have $n = 1$ and dominant $m = 1$ mode numbers for all sawtooth types. This suggests that all the different sawtooth relaxation cycles could be reproduced by a single model. The detailed dynamics of the magnetic island, associated with the resistive internal kink mode, is described by the displacement function, $\xi(t)$ [10], which is inferred from the experimental data for the different sawtooth types.

In triangular sawteeth, obtained with on-axis heating, the $m/n = 1$ mode develops immediately before the crash, whereas, when the deposition is off-axis but still within the sawtooth inversion surface, it grows early in the sawtooth ramp and remains at a saturated level until the sawtooth crash, resulting in saturated sawteeth. In both cases, the sawtooth crash is consistent with a full

reconnection process and its overall effect is to expel particles and heat from the plasma center resulting in a flattening of both the electron temperature and density profiles. In the case of on-axis heating, the formation of a hot ring around the sawtooth inversion surface is observed at the end of the reconnection process. The hot ring forms only when the pre-crash electron temperature profile is sufficiently peaked, as in the case for on-axis ECH deposition. When the ECH power is deposited slightly off-axis, this condition is often not fulfilled and the hot ring is not observed.

With ECH power deposited close to the sawtooth inversion surface, improved stability against the internal kink mode is obtained, leading to a long period of relative MHD quiescence and to pre-crash electron temperature profiles which are flat or even hollow inside the $q = 1$ region. The subsequent sawtooth crash, observed during giant and humpback sawteeth, results in a small variation of the central electron temperature, which shows similar temporal evolution, despite a large difference in the electron density behavior. This difference is not yet understood, but may be ascribed to the ECH associated pump-out. The post-crash electron temperature profiles in both sawtooth types are not poloidally symmetric, indicating an incomplete magnetic reconnection process.

The different types of sawteeth have been simulated using a numerical code based on a theoretical model [10] which describes the evolution of the electron temperature in the presence of localized heat sources and of an $m/n = 1$ magnetic island whose temporal evolution is inferred from the experimental displacement function, $\xi(t)$. Despite the relative simplicity of this model, the simulated sawtooth shapes under the different heating conditions are in agreement with the experimental observations.

7 Acknowledgements

The authors wish to thank Dr. K.A. Razumova for useful discussions and the entire TCV team for their help in this study. This work was partly supported by the Swiss National Science Foundation. F. Porcelli was supported in part by the Italian National Research Council (CNR).

References

[1]Lopez-Cardozo, N.J., et al., Phys. Rev. Lett. **73** (1994) 256.

[2]Cima, G., et al., Plasma Phys. Control. Fusion **40** (1998) 1149.

[3]Hofmann, F., et al., Plasma Phys. Control. Fusion **36** (1994) B277.

[4]Pietrzyk, Z.A., et al., Nucl. Fusion **39** (1999) 587.

[5]Razumova, K.A., et al., Plasma Physics Reports **23** (1997) 13.

[6]Goodman, T.P., et al., in Radiofrequency Heating and Current Drive of Fusion Devices, (Proc. 2nd Europhys. Top. Conf. Brussels, 1998), Vol. 22A, European Physical Society, Geneva (1998) 249.

[7]Pochelon, A., et al., Nucl. Fusion **39** (1999) 1807.

[8]Goodmann, T.P., et al., in International Congress on Plasma Physics (Proc. Cong. Prague, 1998), Vol. 22C, European Physical Society, Geneva (1998) 1324.

[9]Porcelli, F., Rossi, E., Cima, G., Wootton, A., Phys. Rev. Lett. **82** (1999) 1458.

[10]Coppi, B., et al., Fiz. Plasmy **2** (1976) 961 [English translation: Sov. J. Plasma Phys. **1** (1976) 389].

[11]Anton, M., et al., Plasma Phys. Control. Fusion **38** (1996) 1849

[12]Dudok de Wit, T., Pecquet, A.L., Vallet, J.C., Lima, R., Phys. Plasmas **1** (1994) 3288.

[13]Snider, R.T., et al., Phys. Fluids B **1** (1989) 404.

[14]Behn, R., et al., Proc. 7th Int. Symp. Laser Aided Plasma Diagnostics, Fukuoka, Japan (1995) 392.

[15]Smith, G., et al., Proc. 9th Joint Workshop and Electron Cyclotron Heating, Borrego Springs,

Editor: John Lohr, Publisher: World Scientific (1995) 651.

[16]Hanada, K., et al., Phys. Rev. Lett. **66** (1991) 1974.

[17]Goodman,T.P., et al., in Proc. 27th EPS Conf. on Contr. Fusion and Plasma Phys., Maastricht, 1999, paper P3-031.

[18]Weisen, H., et al., Nucl. Fusion **37** (1997) 1741.

[19]Weisen, H., Pasini, D., Weller, A., Edwards, A. W., Rev. Sci. Instrum. **62** (1991) 1531.

[20]Furno, I., et al., in Controlled Fusion and Plasma Physics (Proc. 26th EPS Maastricht , 1999), Vol. 23J ed B. Schweer, G. Van Oost and E. Vietzke (Mulhouse) 1069.

[21]Snider, R.T., et al., Phys. Fluids B **1** (1989) 404.

[22]Levington, F.M., et al., Phys Rev. Lett. **72** (1994) 2895.

[23]Bhatnagar, V.P., et al., Nucl. Fusion **34** (1994) 1579.

[24]Sauter, O., et al., in Theory of Fusion Plasmas (Proc. Workshop Varenna, 1998), Editrice Compositori, Bologna (1998).

[25]Kadomtsev, B.B., Fizika Plazmy **1** (1975) 710; Sov. J. Plasma Phys. **1** (1976) 389..

[26]W. Park and D. A. Monticello, Nucl Fusion **30**, 2413 (1990).

[27]Lichtenberg, A.J., Nucl. Fusion **24** (1984) 1277.

[28]O'Rourke, J., Plasma Phys. Control. Fusion **33** (1991) 289.

[29]West, W.P., Thomas, D.M., de Grassie, J.S., Zheng, S.B., Phys. Rev. Lett. **58** (1987) 2758.

[30]Waelbroeck, F.L., Phys. Plasmas **4**, (1999) 1208.

[31]Porcelli F., et al., submitted for publication in Nucl. Fusion

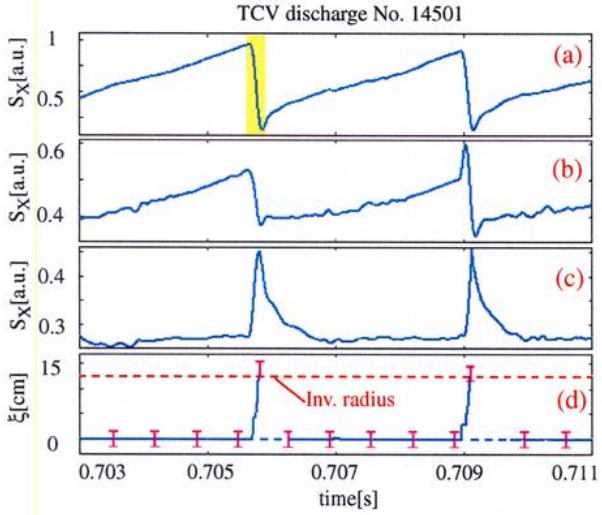

Fig. 1 Evolution of the soft X-ray emissivity at different radial positions, r, during triangular sawteeth in TCV discharge No. 14501: (a) on-axis, $r = 0$; (b) just inside the inversion radius, $r = 0.82 \cdot r_{inv}$; (c) just outside the inversion radius, $r = 1.21 \cdot r_{inv}$; (d) the hot core radial displacement $\xi(t)$ (blue line) together with the sawtooth inversion radius (red, dashed line). The position of the hot core is not shown immediately after the sawtooth collapse since it is not well defined.

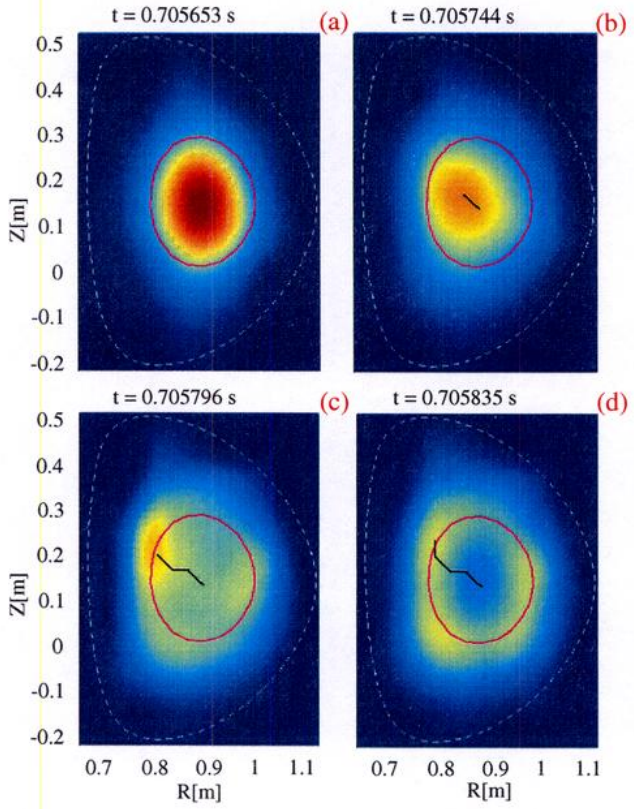

Fig. 2 Series of tomographic reconstructions of the soft X-ray emissivity, during the phase of the sawtooth crash highlighted in yellow in Fig. 1. The hot core displacement (b, c) and the formation of the hot ring (d) are shown. The units are normalized and the color scale is such that red and blue correspond respectively to high and low emissivities. The LCFS is shown as a white, dashed line and the sawtooth inversion surface as a magenta line. The superimposed black line indicates the hot core trajectory from its position before the instability develops to the position corresponding to the time at each frame.

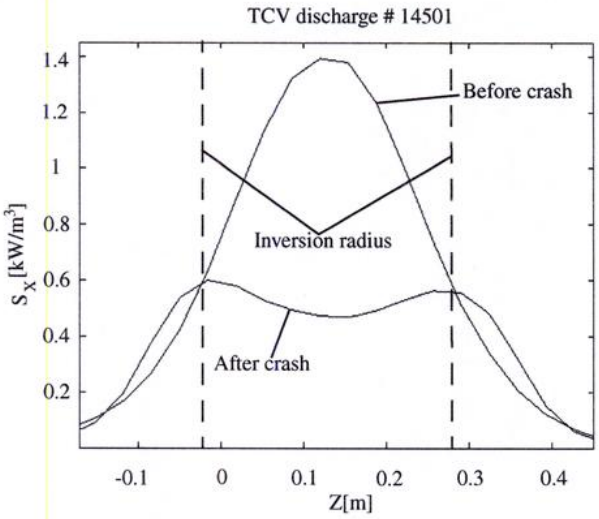

Fig. 3 Soft X-ray emissivity profiles along a central, vertical cut showing the result of the crash for a triangular sawtooth with on-axis ECH power deposition. The position of the sawtooth inversion radius is shown as dashed lines.

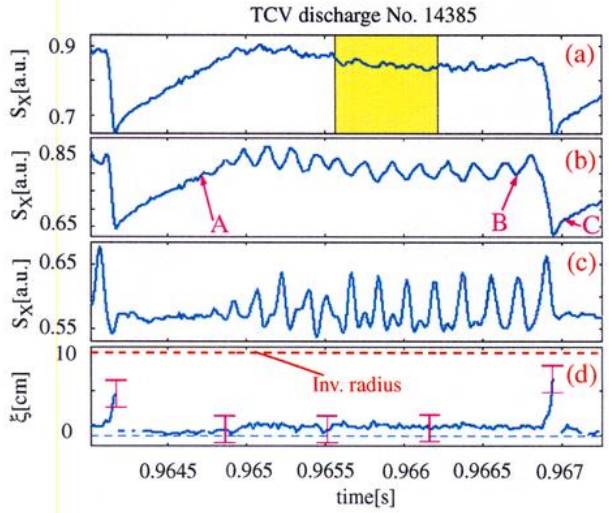

Fig. 4 Time evolution of the soft X-ray emissivity at different radial positions, r, during a saturated sawtooth in TCV discharge No. 14385: (a) close to the magnetic axis, $r = 0.02 \cdot r_{inv}$; (b) slightly off-axis, $r = 0.28 \cdot r_{inv}$; (c) just inside the inversion radius, $r = 0.9 \cdot r_{inv}$, where the frequency doubling is clearly visible; (d) the hot core radial displacement $\xi(t)$ (blue line) together with the sawtooth inversion radius (red, dashed line) are shown. The position of the hot core is not shown immediately after the sawtooth collapse since it is not well defined.

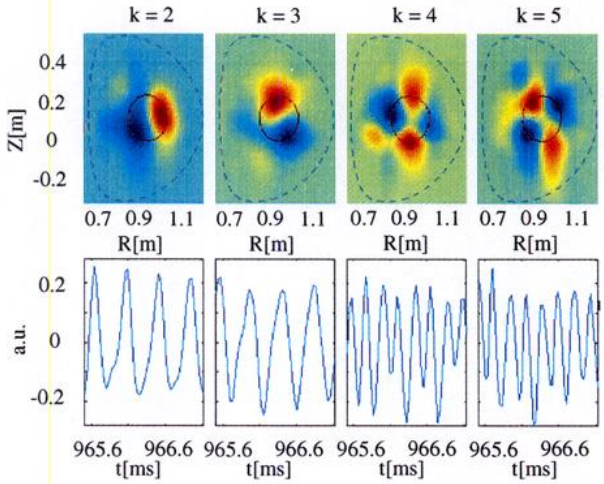

Fig. 5 SVD analysis of the reconstructed soft X-ray emissivity distribution during the saturated phase of the sawtooth, highlighted in yellow in Fig. 4. Shown are the topo/chrono pairs corresponding to the second to fifth largest eigenvalues, $S_{k=2,3,4,5}$. The top row shows the spatial eigenmodes (topos) with the LCFS (dashed black line) and the sawtooth inversion radius (red line). The corresponding temporal eigenvectors (chronos) are shown in the bottom row.

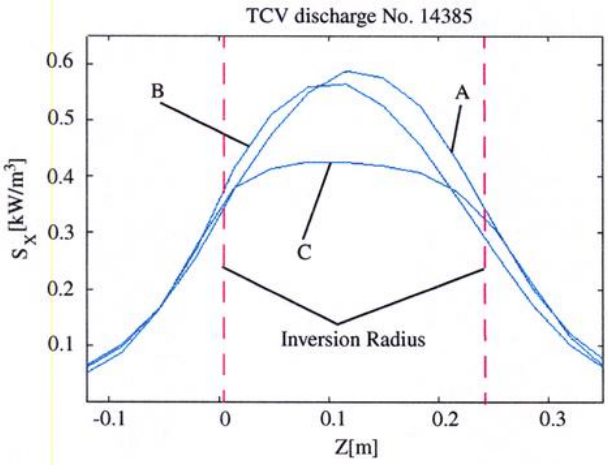

Fig. 6 Soft X-ray emissivity profiles along a central, vertical cut corresponding to the different times indicated by the arrows in Fig. 4. A: the S_X profile is poloidally symmetric at the end of the sawtooth ramp before the instability develops. B: during the sawtooth saturated phase the profile is not poloidally symmetric and the hot core is displaced by ~1 cm from its position before the onset of the oscillations. C: immediately after the sawtooth crash, $t - t_{crash} \sim 0.005 \cdot \tau_{saw}$, the poloidal symmetry is restored. Dashed lines indicate the position of the sawtooth inversion radius.

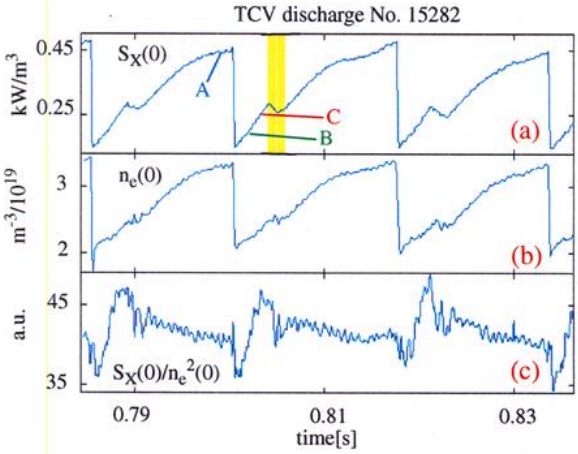

Fig. 7 Giant sawteeth during TCV discharge No. 15282 with ECH power deposited close to the sawtooth inversion surface: (a) the central inverted soft X-ray emissivity, $S_X(0)$; (b) *the central electron density,* $n_e(0)$; *(c) a signal proportional to the variation of the electron temperature,* $S_X(0)/n_e^2(0)$.

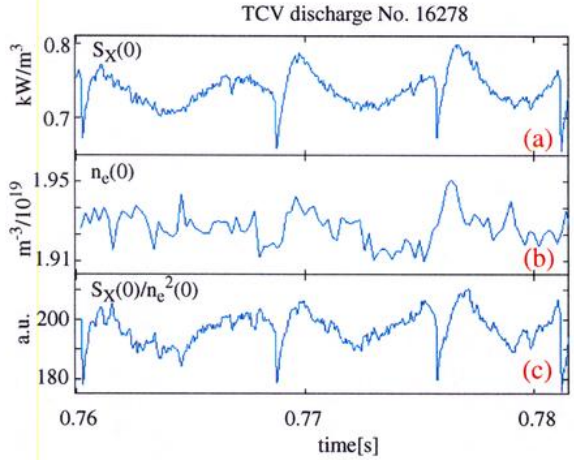

Fig. 8 Humpback relaxation oscillations obtained with ECH power deposited close to the sawtooth inversion surface in TCV discharge No. 16278: (a) central inverted soft X-ray emissivity, $S_X(0)$; *(b) central electron density,* $n_e(0)$; *(d) a signal proportional to the variation of the electron temperature,* $S_X(0)/n_e^2(0)$.

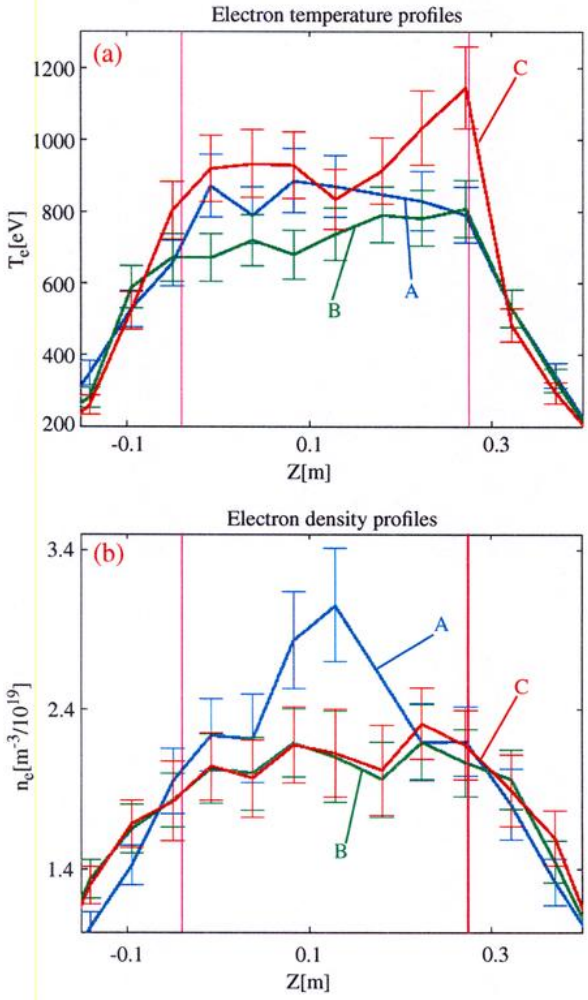

Fig. 9 Thomson scattering profiles for TCV discharge No. 15282, shown in Fig. 7. The electron temperature (a) and the electron density (b) profiles relative to the times, t, indicated by colors in Fig. 7: $t_A = 0.8004$ s, just before the sawtooth crash; $t_B = 0.8014$ s, early during the sawtooth ramp; $t_C = 0.8024$, before the onset of the oscillations. The position of the sawtooth inversion radius, from reconstructed soft X-ray emissivity, is shown in magenta.

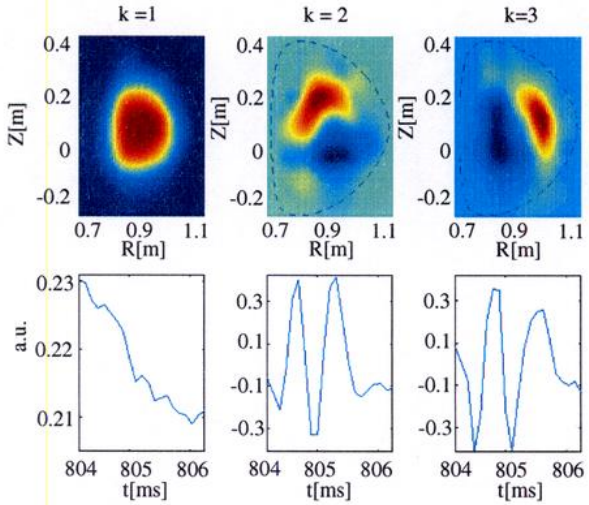

Fig. 10 SVD analysis of the reconstructed soft X-ray emissivity distribution during the phase of the giant sawtooth highlighted in yellow in Fig. 7. The top row shows the spatial eigenmodes (topos) with the LCFS (black dashed line). The corresponding temporal eigenvectors (chronos) are shown in the bottom row.

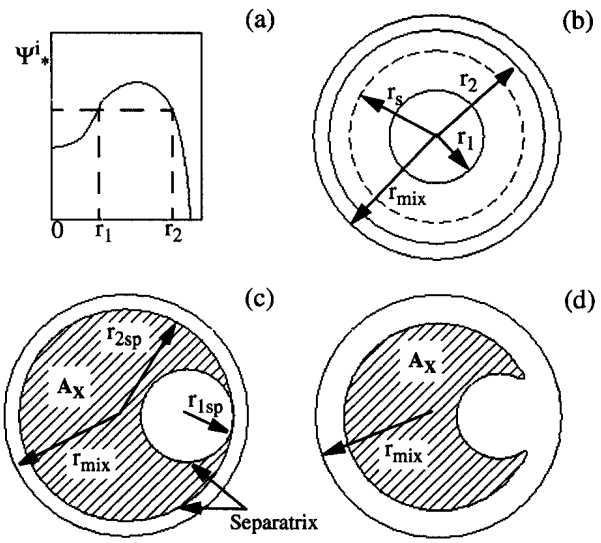

Fig. 11 Magnetic reconnection process according to the Kadomtsev model: (a) pre-crash helical flux for a monotonic q profile; (b) helical flux surfaces before reconnection starts; (c) the flux surface originally at $r = r_1$ reconnects with the flux surface, corresponding to the same helical flux, originally at $r = r_2$; (d) at a later time, the separatrix of (c) has deformed into a crescent-shaped surface maintaining a constant area A_X.

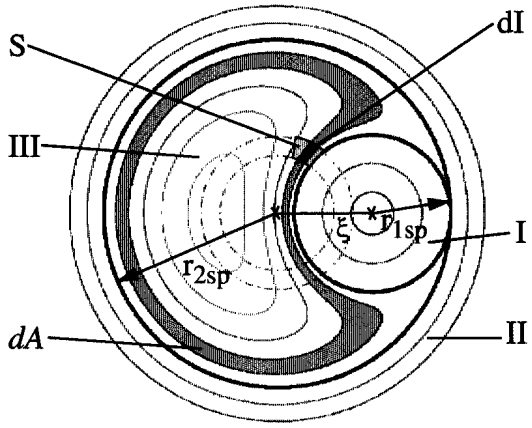

Fig. 12 Magnetic topology during the reconnection. The island separatrix is formed by the circles of radii, r_{1sp} and r_{2sp} and S is the region where the ECH power is deposited. Outside the island separatrix (regions I and II) the magnetic flux surfaces are circular while inside (region III) they are crescent shaped. In the plasma rest frame, with the assumption of rigid toroidal rotation, the heated region is a ring indicated by dot-dashed circles. dI shows the intersection of the heated ring with a generic flux tube of cross sectional area dA.

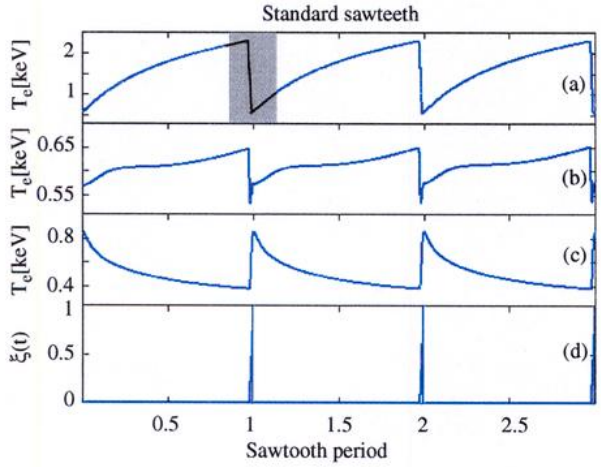

Fig. 13 Simulation of triangular sawteeth with on-axis ECH power deposition. The electron temperature is shown at different radial positions: (a) on-axis, $r = 0$; (b) just inside the inversion radius, $r = 0.85 \cdot r_{inv}$; (c) just outside the inversion radius, $r = 1.27 \cdot r_{inv}$; (d) displacement function $\xi(t)$.

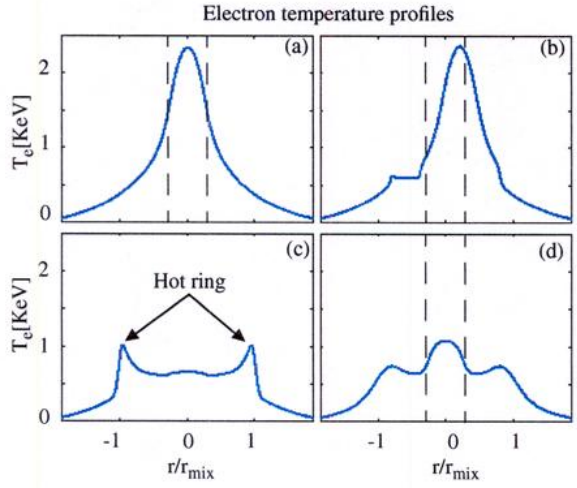

Fig. 14 Simulated electron temperature profiles for the time window indicated in Fig. 13: (a) pre-crash, $\xi = 0$; (b) during hot core displacement, $\xi = 0.41$; (c) just after the sawtooth crash, $\xi = r_{mix}$, the hot ring is formed; (d) early during reheat ramp, corresponding to $t - t_{crash} = 0.125 \cdot \tau_{saw}$. The power deposition region is shown as dashed lines.

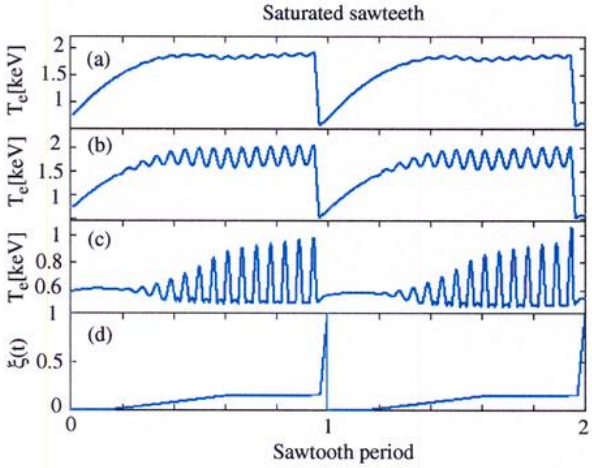

Fig. 15 Simulation of saturated sawtooth with on-axis ECH power deposition. The electron temperature is shown at different radial positions: (a) close to the magnetic axis, $r = 0.01 \cdot r_{inv}$; (b) slightly off-axis, $r = 0.15 \cdot r_{inv}$; (c) just inside the inversion radius, $r = 0.85 \cdot r_{inv}$, where the frequency doubling is visible; (d) the hot core radial displacement $\xi(t)$.

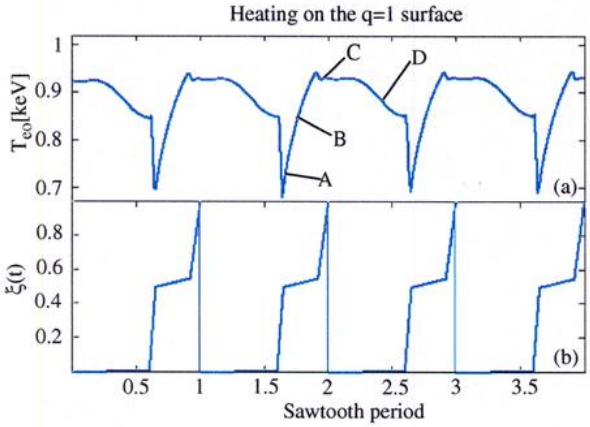

Fig. 16 Simulation results of sawtooth oscillations with ECH power deposited close to the $q = 1$ surface: (a) the central electron temperature; (b) the displacement function $\xi(t)$.

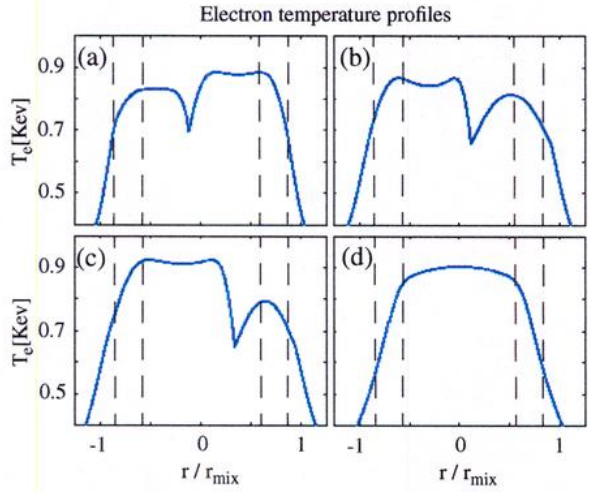

Fig. 17 Simulated electron temperature profiles obtained with ECH power deposited on the $q = 1$ *surface. The* T_e *profiles shown in (a, b, c, d) correspond respectively to the times A, B, C, D indicated in Fig. 16: (a, b) post-crash profiles during the sawtooth ramp,* $\xi = 0.5$, $\xi = 0.518$; *the profile are not poloidally symmetric since the reconnection process is incomplete; (c) during hot core displacement,* $\xi = 0.719$; *(d) at complete magnetic reconnection,* $\xi = 1$. *The power deposition region is shown by dashed lines.*